Volume 16
Number 5
7 February 2024
Pages 2063-2674

Nanoscale

rsc.li/nanoscale

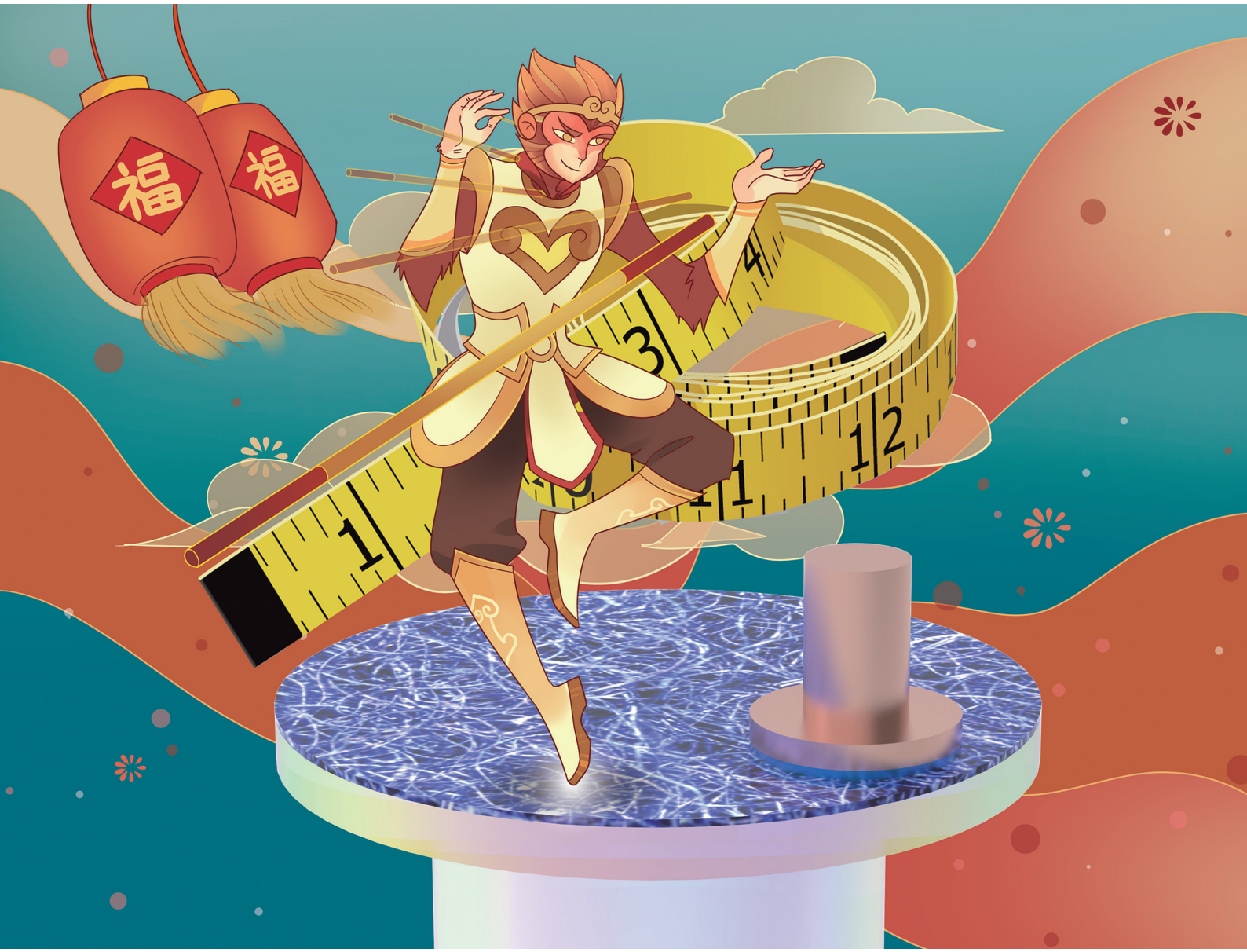

ISSN 2040-3372

ROYAL SOCIETY OF CHEMISTRY

PAPER
Zhenyu Zhang *et al.*
Atomic surface achieved through a novel cross-scale model from macroscale to nanoscale

NCNST

Nanoscale

PAPER

View Article Online
View Journal | View Issue

Check for updates

Cite this: *Nanoscale*, 2024, **16**, 2318

Atomic surface achieved through a novel cross-scale model from macroscale to nanoscale

Feng Zhao,[a] Zhenyu Zhang, *[a] Xingqiao Deng,[b] Junyuan Feng,[c] Hongxiu Zhou,[d] Zhensong Liu,[a] Fanning Meng[c] and Chunjing Shi[c]

Chemical mechanical polishing (CMP) is widely used to achieve an atomic surface globally, yet its cross-scale polishing mechanisms are elusive. Moreover, traditional CMP normally employs toxic and corrosive slurries, resulting in potential pollution to the environment. To overcome these challenges, a novel cross-scale model from the millimeter to nanometer scale is proposed, which was confirmed by a newly developed green CMP process. The developed CMP slurry consisted of hydrogen peroxide, sodium carbonate, sodium hydroxycellulose, and silica. Prior to CMP, fused silica was polished by a ceria slurry. After CMP, the surface roughness (S_a) was 0.126 nm, the material-removal rate was 88.3 nm min^{-1}, and the thickness of the damaged layer was 8.8 nm. The proposed model was built by fibers, through integrating Eulerian and Lagrangian models and reactive force field-molecular dynamics. The results predicted by the model were in good agreement with those of CMP experimentally. A model for large-sized fibers revealed that a direct contact area of 11.12% was obtained for a non-woven polishing pad during the CMP experiments. Another model constructed *via* combining Eulerian and Lagrangian functions showed that the stress at the intersections of the fibers varied mainly from 0.1 to 0.01 MPa and was higher than the stress at other parts. An increase in viscosity led to a decrease in the areas with low stress, demonstrating that viscosity enhanced the stress and facilitated the removal of material. At the microscale and nanoscale, the stress of the abrasive surface exposed to the workpiece changed from 2.21 to 6.43 GPa. Stress at the interface contributed to the formation of bridging bonds, further promoting the removal of material. With increasing the compressive stress, the material-removal form was transformed from a single atom to molecular chains. The proposed model and developed green CMP offer new insights to understand the cross-scale polishing mechanism, as well as for designing and manufacturing novel polishing slurries, pads, and setups.

Received 19th October 2023,
Accepted 19th December 2023

DOI: 10.1039/d3nr05278h

rsc.li/nanoscale

Published on 04 January 2024. Downloaded by Yunnan University on 8/15/2025 7:01:03 AM.

1. Introduction

Chemical mechanical polishing (CMP) integrates mechanical loading and chemical dissolution and is currently considered as the foremost way to achieve global nanoscale flattening.[1–5] In practice, the removal mechanism of different materials is still unclear and the CMP performance is usually directly dependent on the experience of the operator and massive experiments, which leads to an extreme waste of resources, higher cost, and pollution.[6–8] Therefore, a full-analysis strategy is ungently required for addressing the diverse challenges of future polishing materials and process requirements.

In the CMP process, the material-removal mechanism is an intricate multiscale process.[9,10] In general, this process involves the transmission of forces from nanoscale abrasives to a microscale polishing pad, subsequently mediated by macroscale polishing fluids, culminating in the removal of atomic-scale material from a workpiece surface.[11–13] The CMP exemplifies a compelling interplay of mechanical and chemical factors, the modulation of which is contingent upon an array of influential parameters. Notably, the quantification of the material removal and damage mechanisms within CMP remains a formidable challenge when relying solely on experimental methodologies.[12,14–16] Presently, due to limitations of the testing techniques, the material-removal mechanism in the CMP process can only be observed and captured to a limited extent.[17,18] Predominantly, extant research endeavors

[a]*State Key Laboratory of High-performance Precision Manufacturing, Dalian University of Technology, Dalian 116024, China. E-mail: zzy@dlut.edu.cn*
[b]*School of Mechanical and Electrical Engineering, Chengdu University of Technology, Chengdu 610059, China*
[c]*School of Mechanical Engineering, Hangzhou Dianzi University, Hangzhou 310018, China*
[d]*School of Energy and Power Engineering, Dalian University of Technology, Dalian 116024, China*

This journal is © The Royal Society of Chemistry 2024

Published on 04 January 2024. Downloaded by Yunnan University on 8/15/2025 7:01:03 AM.

have been predominantly focused on postulating mechanisms based on intricate experimental characterizations, which is a resource-intensive and intricate approach.

As a promising avenue, numerical simulation offers another direction to explore the CMP material-removal mechanism from different scales, mainly including finite element analysis (FEM),[19–21] computational fluid mechanics (CFD),[22–24] smooth particle hydrodynamics (SPH),[25–27] and molecular dynamics (MD).[28–31] Among these, the FEM, CFD, and SPH approaches mainly focus on the macro- and mesoscale aspects and the chemical reactions in CMP are not considered. Besides, due to the great difficulty in constructing physical models, the nonlinear topological structure of the polishing pad is often neglected, thus oversimplify the calculation and leading to a deviation in the results.[12,32,33] The complex fluid–solid coupling effect between the pad and slurry, stress-diffusion transport mechanism, and abrasive stress level on fibers resulting from structural nonlinearity have yet to be investigated. Instead, MD can demonstrate the dynamic process of the polishing system at the atomic scale.[29,34] Conventional MD is based on Newtonian equations and displays great limitations.[35,36] As a type of extension, reactive force field-molecular dynamics (ReaxFF-MD) breaks through the classic system and introduces a description of the chemical reactions into the potential function by introducing the relationship between the bond order and potential function.[37,38] The ReaxFF-MD method has been successfully applied for revealing the microscopic material-removal mechanism of different materials (Cu, fused silica, and diamond) under different working conditions.[39–42] However, the above studies are based on single sides of an aspect with significant scale limitations that do not allow for in-depth mechanism investigations.[43–45] Despite the extensive exploration of the CMP-removal mechanisms by researchers, there are still notable issues that are yet to be resolved, including macroscopic to microscopic scale mapping, and microscopic to nanoscopic scale mapping.

From a macroscopic mapping point of view, the contact situation of polishing pads is highly complex and nonlinear. It is susceptible to influence the mechanical properties of the surface layer and the microscopic morphology. Most of the current research ignores the coupling between the contact interface between the polishing pad, slurry, and workpiece. Therefore, it is impossible to precisely reveal the stress-carrying and -transfer characteristics of polishing pads; yet it is important to explain the magnitude and distribution of the stresses under the microscopic contact conditions, as well as the influence on the material-removal process. From a microscopic mapping aspect, the coupling removal mechanism from the microscopic abrasive to nano atoms is still unclear. Although series research has been conducted to investigate the removal rule under MD approaches, the simulation conditions differ greatly from the actual working conditions. Accurate boundary conditions from microscopic abrasives are difficult to obtain and apply to nanoscale calculations, which subsequently leads to inaccurate calculations. These two intricate issues represent great challenges for mapping the complex macroscopic polishing process parameters for the nanoscale removal, thereby impeding developing comprehensive mechanism guidance and further atomic-level flattening process optimization.

In this work, a full-scale (from mm to nm) mapping analysis strategy (FSMAS) integrating a large-sized fiber model, coupled Eulerian and Lagrangian (CEL), and ReaxFF-MD technology was first proposed to investigate the nonlinear viscosity effect on fused silica material removal combined with CMP experiments. In our FSMAS, the nonlinear topological structure of the non-woven polishing pad, nonlinear constitution of the slurry, and nanoscale chemical reactions were simultaneously considered. This first such proposed mapping analysis strategy is of great significance to realize accurate quantitative prediction and for process stability analysis of the CMP process.

2. Experimental details

2.1. Chemical mechanical polishing experiments

Polished fused silica samples (10 mm × 10 mm × 4 mm) were purchased from Donghai County Weida Quartz Products Co., Ltd (China) and applied in CMP. All the CMP experiments were performed on a UNIPOL-1502 polishing machine from Shenyang Kejing Automation Equipment Co., Ltd, (China). In this experiment, D-sorbitol from Shanghai Aladdin Biochemical Technology Co., Ltd (China), sodium carbonate (Na_2CO_3), and 30% hydrogen peroxide solution (H_2O_2) from Sinopharm Chemical Reagent Co., Ltd (China) were employed as the dispersant, a pH regulator, and an oxidant, respectively. To quantitatively evaluate the effect of viscosity on the CMP, sodium hydroxycellulose (CMC-Na) was selected as a viscosity regulator. Before the CMP, three samples were evenly distributed and glued on cast iron disks (8 cm in diameter). Then, 500 mL of rough polishing slurry (S0) with ceria abrasives (3 μm CeO_2) from Jinan Zhongye New Materials Co., Ltd (China) was utilized to roughly Polish the fused silica samples for 1 h to obtain similar original quartz surfaces and avoid sub-surface damage that would be difficult to repair. Then, different polishing slurries (S1–S3) were employed respectively in the subsequent CMP experiments. The detailed polishing slurry and process parameters are shown in Tables 1 and 2. The polishing machine (UNIPOL-1200S) used for polishing and the non-woven polishing pad were purchased from Shenyang Kejing Automation Equipment Co. After CMP, the

Table 1 Composition of the slurries for the rough and fine polishing

Slurry	Composition
S1	3 wt% SiO_2 + 5 wt% H_2O_2 + 0.4 wt% Na_2CO_3
S2	3 wt% SiO_2 + 5 wt% H_2O_2 + 0.4 wt% Na_2CO_3 + 0.3 wt% CMC-Na
S3	3 wt% SiO_2 + 5 wt% H_2O_2 + 0.4 wt% Na_2CO_3 + 0.6 wt% CMC-Na

Published on 04 January 2024. Downloaded by Yunnan University on 8/15/2025 7:01:03 AM.

Table 2 Process parameters for the rough and fine polishing

Tests	Pressure	Speed	Flow rate	Polishing time
Rough polishing	27.5 kPa	90 rpm	15 ml min^{-1}	30 min
Fine polishing	37.5 kPa	80 rpm	25 ml min^{-1}	30 min

glycol and complexes were removed by an ethanol rinse and a clean surface was obtained by compressed air drying.

2.2. Characterization

Scanning electron microscopy (SEM, JSM-7800F, Japan) was utilized for characterization of the silica abrasives' morphology. The surface quality of the polished and unpolished fused silica was observed using an optical microscope (MX40, Olympus, Japan). The material-removal rate (MRR) of the CMP was calculated by measuring the mass difference between the unpolished and polished samples using a precision balance. The surface roughness of the 3D morphology of fused silica after CMP was measured using a non-contact optical surface profilometer (Zygo NewView™ 9000, USA) and an AFM system (XE-200, Park Systems Corp., South Korea), and the average surface roughness values were obtained from five randomly selected sample points. The rheology analysis of the polishing slurry was conducted at 25 °C and 65% humidity using a rotational rheometer (TA Instruments, US). The shear frequency ranged from 0.1 to 100 Hz with three tests performed and averaged for each mean value. Polished fused silica samples were analyzed by XPS (ThermoFisher, Thermo Scientific K-Alpha+, USA) to investigate the changes in valence states. All the binding energies were referenced to the C 1s peak at 284.8 eV. FTIR measurements (ThermoFisher, 6700, USA) were performed to detect vibrational peaks on the workpiece surface after polishing. The damaged layer of the sample was observed through high-resolution transmission electron microscopy (HRTEM) imaging (Talos F200x, USA). Prior to the TEM observations, the cross-sectional samples were prepared by focused ion beam milling from the polished surface.

2.3. Full-scale numerical analysis strategy

In this work, the FSMAS was first put forward for quantitatively investigating the material-removal mechanism in different scales. Fig. 1 exhibits the proposed strategy, which includes four different scales, namely the macro (mm), meso (mm–μm), micro (μm–100 nm), and nano scale (0.1–100 nm) across six orders of magnitude (mm–nm). First, the large-sized random fiber polishing pad model was established, and the compression experiment and simulation were conducted to verify the consistency of the model. Then, considering that the fluid–structure (FSI) effect would greatly increase the numeri-

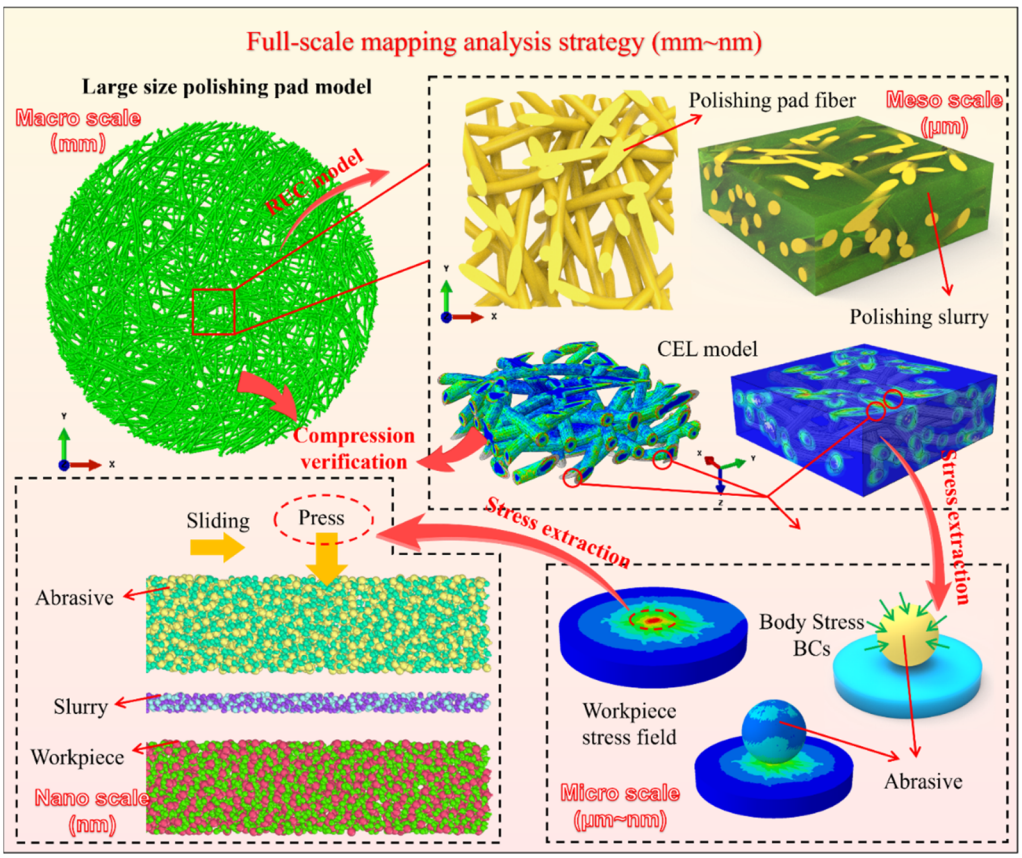

Fig. 1 Proposed full-scale mapping analysis strategy.

This journal is © The Royal Society of Chemistry 2024

Published on 04 January 2024. Downloaded by Yunnan University on 8/15/2025 7:01:03 AM.

cal calculation cost, the RUC model containing both the polishing pad and slurry was further established by selecting a typical area. Different from previous FSI models, the established polishing models experience a large deformation of solid materials, which creates great difficulties for conventional computational fluid dynamics (CFD) approaches to deal with. Therefore, the coupled Eulerian–Lagrangian approach (CEL) was applied in our new model.[22,46,47] In addition, it is worth noting that to evaluate the effect of different fluids on the polishing effect, a nonlinear constitution of the slurry was also considered in the model. In the mesoscale calculation results, the characteristic stress on the fibers and slurry was then extracted as the input boundary conditions for a smaller microscale abrasive model. Through this logical iteration, the direct contact force of the workpiece exerted by the abrasive resulting from the joint action of the polishing pad and slurry could be precisely calculated. Finally, the characteristic stress on the workpiece was further applied as the input boundary condition of the nanoscale ReaxFF-MD model. Through ReaxFF-MD, the changes from the chemical reactions resulting from the contact stress could be quantitatively evaluated. In previous MD models, the input press was usually set to a fixed imaginary value, which could lead to one-sided results. The full-scale analysis strategy proposed here utilizes stress relationships as the bridge between different scales and validates the model's accuracy through coordination with corresponding macroscopic experiments.

This logical iterative full-scale analysis strategy can well establish relationships between different scales. Through this strategy, the boundary condition input problem of the microscopic model could be well solved. The interactions between the different components in CMP were accurately captured, including the interaction between the solid and nonlinear fluid, and the coordination mechanism of the chemical field and force field.

2.4. Large-sized random fiber polishing pad model

Compared with other polishing pads, the non-woven polishing pad exhibits a wide range of applicability, durability, and designability. Therefore, the non-woven polishing pad was selected as a typical research object. However, due to its complex nonlinear topology, as presented in Fig. 2(a), it presents great difficulty for constructing an accurate geometric model.[48–50] In this work, the spatial layering growth approach was applied to establish the geometric model for the polishing pad by script,[51] with the detailed modeling steps illustrated in Fig. 3(a) while the established model is shown in Fig. 2(b) and (c). After convergence debugging, the polishing pad model was broken down into 1028509 B31 elements. The contact between fibers was handled by the general contact algorithm of

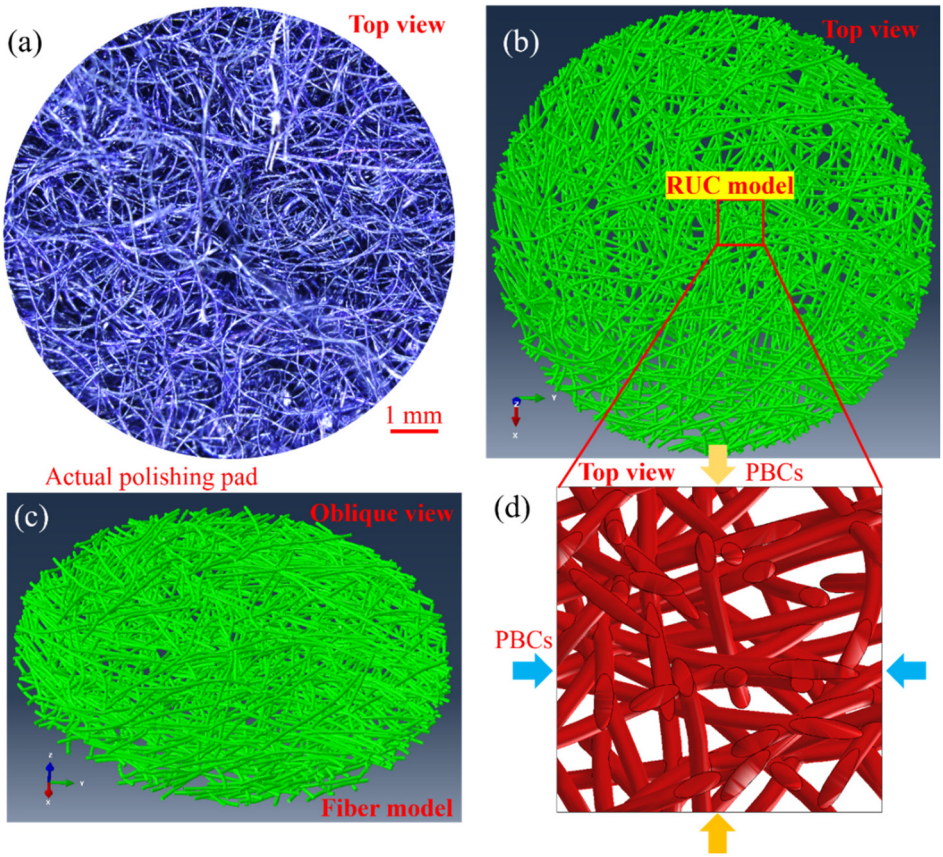

Fig. 2 Large-sized non-woven polishing pad and its numerical fiber model: (a) actual polishing pad structure, (b) and (c) the established large-sized polishing pad model in different views, (d) the non-woven RUC model and its periodic boundary condition selected generated in this work.

Published on 04 January 2024. Downloaded by Yunnan University on 8/15/2025 7:01:03 AM.

Coulomb's law of friction. The fiber coefficient of friction was set as 0.3 in Abaqus/Explicit.[52]

2.5. Mesoscale fluid–structure interaction model

In CMP processes, the interaction between the polishing pad and slurry demonstrates a great significance for the formation of ultrasmooth surfaces. To be specific, the material-removal force of the abrasive on the workpiece originates from the interaction between the polishing pad and slurry. However, this part of research is often overlooked, and the reason is the highly complex structure of the polishing pad and the nonlinear rheology of the polishing slurry. In general, it is highly challenging to investigate the interaction between the flexible large deformation pad and polishing fluid from a numerical perspective. To reduce the calculation cost of this work, a repeated unit cell (RUC) model was generated by the same approach applied in Section 3.1 with a size of 100 μm × 100 μm × 30 μm. The RUC polishing pad model exhibited an obvious geometric symmetry in both the X and Y directions, as shown in Fig. 2(d). The coupled Eulerian–Lagrangian (CEL) approach was selected in this work and the fluids and solids were separately established, which enabled large deformations and complex flows in fluids to be considered. The detailed CEL information and calculation rules are presented in Fig. 3(b) and (c).

2.6. Material constitutive modeling

In the model, the fibers are considered as transversally isotropic, and the detailed elastic constants are presented in Table 3, where L denotes fiber direction and T denotes the transverse direction. Material orientation of the fiber elements was set to ensure that the 1 direction of the element follows the fiber/yarn direction. The rheology of the polishing slurry can be controlled by changing the viscosity regulator content, such as sodium methylol cellulose. Three different slurries with different viscosities were developed, and the power law model[53] was selected to express the rheology of the slurries, as presented in eqn (1):

$$\eta = m\dot{\gamma}^{n-1} \quad (1)$$

The flow coefficient m, flow behavior coefficient n, and shear rate η were used to define the dynamic viscosity of the

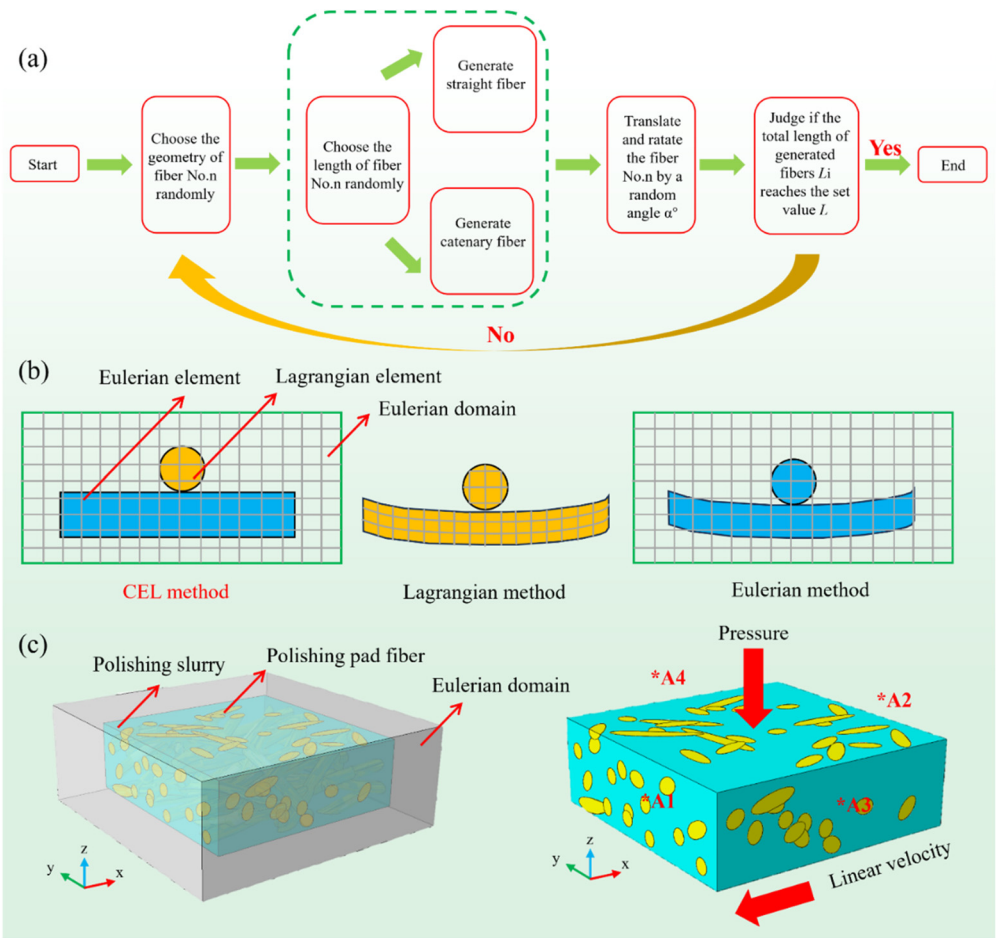

Fig. 3 (a) Script flow of the spatial layering fiber growth model, (b) computational feature of the CEL method compared with the conventional Lagrangian method and Eulerian method, (c) CEL model diagram and boundary conditions.

 This journal is © The Royal Society of Chemistry 2024

Published on 04 January 2024. Downloaded by Yunnan University on 8/15/2025 7:01:03 AM.

Table 3 Elastic properties of the polishing pad fiber

E_L (MPa)	E_T (MPa)	G_{LT} (MPa)	G_{TT} (MPa)	V_{LT}	V_{TT}
800	10	5	3.85	0.3	0.3

slurry in this study. When $n < 1$, the fluid exhibits shear thinning, resulting in a decrease in apparent viscosity with increasing the shear rate. Conversely, when $n > 1$, the fluid exhibits shear thickening, leading to an increase in apparent viscosity with increasing the shear rate. In the case of $n = 1$, the fluid behaves as a Newtonian fluid, where its viscosity remains constant regardless of the changes in the shear rate. The piecewise function method was employed to accurately describe two regions, as defined by eqn (2):

$$\eta(\dot{\gamma}) = \begin{cases} m_1\dot{\gamma}^{n_A-1}, \eta_{min} < \eta < \eta_A \\ m_2\dot{\gamma}^{n_B-1}, \eta_{min} < \eta < \eta_B \end{cases} \quad (2)$$

The segmented characteristics of the power law model are primarily determined by several factors, including the values of each stage m and n, the maximum viscosity, minimum viscosity, and other specific parameter values as presented in Table 4. To define the slurry's viscosity under different rheological regions, the user-defined subroutine VUSDFLD in Abaqus/Explicit was employed.

The hydrostatic behavior of the slurry was expressed by the Mie–Grüneisen equation of state (EOS):[46]

$$p = \frac{\rho_0 C_0{}^2 \chi}{(1 - s\chi)^2}\left(1 - \frac{\Gamma_0\chi}{2}\right) + \Gamma_0 E \quad (3)$$

where $\chi = 1 - (\rho_0/\rho)$, p is the pressure, C_0 is the sound viscosity through the medium, ρ_0 is the initial density, ρ is the current density, Γ_0 is a material parameter, and E is the internal energy per unit reference volume. Then,

$$s = dU_s/dU_p \quad (4)$$

where s is the linear Hugoniot slope, U_s is the shock velocity, and U_p is the particle velocity.

2.7. Periodic boundary conditions

In previous models, the periodic boundary conditions (PBCs) were typically applied to opposite surfaces of the RUC model in a pointwise manner. However, due to the disparity between the fiber model and mesoscale model, the PBCs are here imposed on pairs of nodes within each fiber (Fig. 3(c)) in areas A_1 and A_3 with identical values.[52] These conditions are also enforced on the nodes in area A_2 and their corresponding counterparts in area A_4.

The PBCs on each node pair can be written as follows:

Nodes in areas A_1 and A_3:

$$U_1^{A_1} = U_1^{A_3} + \varepsilon_{12}\cdot\Delta x_2,\ U_2^{A_1} = U_2^{A_3} + \varepsilon_{22}\cdot\Delta x_2,\ U_3^{A_1} = U_3^{A_3} + \varepsilon_{32}\cdot\Delta x_2 \quad (5)$$

Nodes in areas A_2 and A_4:

$$U_1^{A_2} = U_1^{A_4} + \varepsilon_{12}\cdot\Delta x_2,\ U_2^{A_2} = U_2^{A_4} + \varepsilon_{22}\cdot\Delta x_2,\ U_3^{A_2} = U_3^{A_4} + \varepsilon_{32}\cdot\Delta x_2 \quad (6)$$

where U_1, U_2, and U_3 are the displacements in the x, y, and z directions; Δx_1 and Δx_2 are the distances from areas A_1 to A_3 and A_3 to A_3; and ε_{ij} are the components of the macroscopic strain tensor. Eqn (5)and (6) can be complied in Abaqus by the linear equation constraint.

The form of the equation constraint in Abaqus is as follows:

$$A_1U_i^p + A_2U_j^q + \ldots + A_NU_k^r = 0 \quad (7)$$

where U_k^r is the displacement at node P in the i direction, and A_N is a coefficient that defines the relative motion of the nodes. By this method, we introduce two reference points to implement eqn (5)–(7), then the values of the last term in each equation are imposed as displacements on these reference points. The deformation of the models is controlled by the displacements imposed at these points, while the reference points are not connected to any material part.

2.8. Microscale abrasive model

In the microscale model, the interaction between the abrasives and workpiece is investigated by extracting the fiber characteristic stress and fluid characteristic stress from the mesoscale model as input pressure boundary conditions, as shown in Fig. 4(a). After convergence debugging, the workpiece was discretized to 53800 C3D8R elements, while the single abrasive was discretized to 75351 C3D4R elements in Abaqus/Standard. In addition, the workpiece bottom was fixed and the contact between the abrasive and workpiece was handled by a surface-to-surface contact algorithm considering Coulomb's law of friction with a 0.3 friction coefficient.

The Johnson–Holmquist 2 (JH-2) constitutive model was applied to describe the mechanical properties of the workpiece and abrasive.[54,55] In JH-2 constitutive modeling, the material strength is described by a smooth curve as a function of the hydrostatic pressure. The normalized equivalent strength σ^*_{eq},

Table 4 Details of the parameters of different types of fluids

Samples	Minimum viscosity	Maximum viscosity	m_1	m_2	n_A	n_B
S1	0.02395	19.756	0.00468	—	2.81581	—
S2	2.7933	66.315	32.98535	0.03754	0.04691	2.6253
S3	0.9611	33.436	1.66785	0.00964	0.30097	2.7722

Published on 04 January 2024. Downloaded by Yunnan University on 8/15/2025 7:01:03 AM.

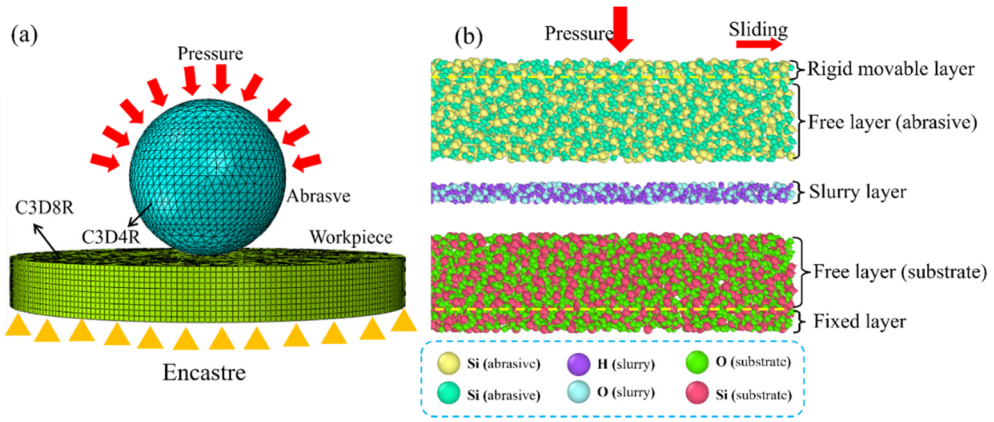

Fig. 4 (a) Microscale model and (b) nanoscale ReaxFF-MD model.

intact strength $\sigma^{*}_{\mathrm{eq},i}$, and fracture are considered as ratios of actual equivalent strength $\sigma^{*}_{\mathrm{eq},f}$ and equivalent strength σ_{eq} at the Hugoniot elastic limit (HEL), and can be written as:

$$\sigma^{*}_{\mathrm{eq}} = \frac{\sigma_{\mathrm{eq}}}{\sigma_{\mathrm{HEL}}} \tag{8}$$

where

$$\sigma^{*}_{\mathrm{eq},i} = \overline{A}\left(P^{*} + \overline{T}^{*}\right)^{\overline{N}}\left[1 + \overline{C}\ln\left(\frac{\dot{\varepsilon}}{\dot{\varepsilon}_0}\right)\right] \tag{9}$$

$$\sigma^{*}_{\mathrm{eq},f} = \overline{B}\left(P^{*}\right)^{\overline{M}}\left[1 + \overline{C}\ln\left(\frac{\dot{\varepsilon}}{\dot{\varepsilon}_0}\right)\right] \tag{10}$$

The maximum normalized fracture strength is defined as $\sigma^{*}_{\mathrm{eq},f,\max}$, $\overline{A}$, $\overline{B}$, $\overline{C}$, $\overline{N}$, and $\overline{M}$ are material inherent parameters, $P^{*} = \frac{P}{P_{\mathrm{HEL}}}$, $\overline{T}^{*}$ equals the normalized maximum tensile pressure $\frac{\bar{T}}{P_{\mathrm{HEL}}}$, and P_{HEL} is the pressure at the HEL.

The strengths of the abrasive and workpiece were assumed to be an affine function of the damage variable ($0 < D < 1$) as described by eqn (11)

$$\sigma^{*}_{\mathrm{eq}} = \sigma^{*}_{\mathrm{eq},i} - D\left(\sigma^{*}_{\mathrm{eq},i} - \sigma^{*}_{\mathrm{eq},f}\right) \tag{11}$$

The damage variable D can be calculated by eqn (12):

$$D = \sum \frac{\Delta\varepsilon^{\mathrm{eff}}_{\mathrm{pl}}}{\varepsilon^{f}_{\mathrm{pl}}} \tag{12}$$

The pressure can be calculated by the following eqn (13):

$$P = \begin{cases} K_1\eta + K_2\eta^2 + K_3\eta^3 + \Delta P, \text{ if } \eta > 0 \\ K_1\eta, \text{ otherwise} \end{cases} \tag{13}$$

In addition, $\varepsilon^{f}_{\mathrm{pl}}$ can be expressed by eqn (14), and the bulging pressure ΔP by eqn (15):

$$\varepsilon^{f}_{\mathrm{pl}} = (P* + \overline{T}*)^{\mathrm{D}_2} \tag{14}$$

$$\Delta P_{t+\Delta t} = -K_1\eta_{t+\Delta t} + \sqrt{\left(K_1\eta_{t+\Delta t} + \Delta P\right)^2 + 2\beta_f K_1 \Delta U} \tag{15}$$

where D_1 and D_2 are material parameters, and the detailed parameters are presented in Table 5.

2.9. Nanoscale ReaxFF-MD model

The ReaxFF-MD model includes five parts: the rigid layer, abrasive free layer, slurry layer, substrate free layer, and fixed substrate layer (Fig. 4(b)). Here, both the substrate and abrasive materials were fused silicas, and the polishing slurry contained 500 H_2O molecules and 15 H_2O_2 molecules. The substrate was composed of 3200 Si and 6400 O atoms and the overall size of the model was 57.2 Å × 57.2 Å × 100 Å. The Si/O/H potential function developed by Fogarty was employed to simulate the interatomic interactions of the system. The time-step was set as 0.25 fs, the X and Y directions were set as periodic boundaries, and the Z direction was set as a fixed boundary. All the simulations of this model were conducted under the NVT ensemble. The Nosé–Hoover thermostat was used to

Table 5 The detailed JH-2 constitutive parameters in this work

ρ	G (MPa)	$\overline{A}$	$\overline{N}$	$\overline{B}$	$\overline{M}$	FS
2200 kg m^{-3}	30 980	0.93	0.77	0.2	1.0	1.0
$\overline{N}$	β_f	$\overline{T}$ (MPa)	$\sigma^{\max}_{f}$	HEL (MPa)	P_{HEL} (MPa)	D_1
0.003	1.0	150	0.5	5950	2920	0.043
D_2	K_1 (MPa)	K_2 (MPa)	K_3 (MPa)			
0.85	45 400	−138 000	290 000			

This journal is © The Royal Society of Chemistry 2024

Published on 04 January 2024. Downloaded by Yunnan University on 8/15/2025 7:01:03 AM.

keep the system temperature at about 300 K. The CMP process was simulated in following four steps:

(1) The system was relaxed for 100 ps to achieve a sufficient reaction between the slurry and interface. (2) The rigid layer was controlled to drive the abrasive to move along the Z axis at 40 m s^{-1} for 50 ps. Then, a change curve of the Z-axis downforce during the pressing process was generated, and different pressure levels were selected to simulate the

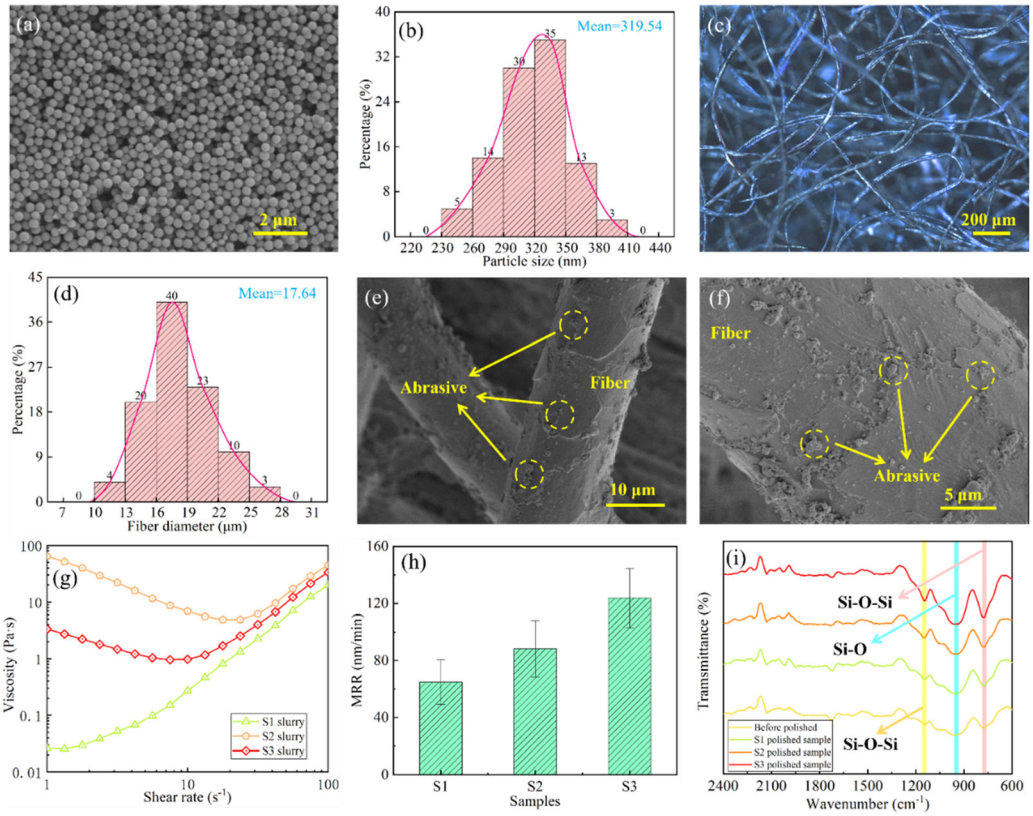

Fig. 5 (a) SEM image of the abrasive SiO_2 used in this work, (b) size distribution of the SiO_2 abrasives, (c) optical morphology of the polishing pad fiber used in this work, (d) fiber diameter of the polishing pad, (e) and (f) surface morphology of the polished pad fiber, (g) dynamic rheology of three developed slurries, (h) material-removal rates of the different slurry samples, (i) infrared spectra of the before and after polished samples.

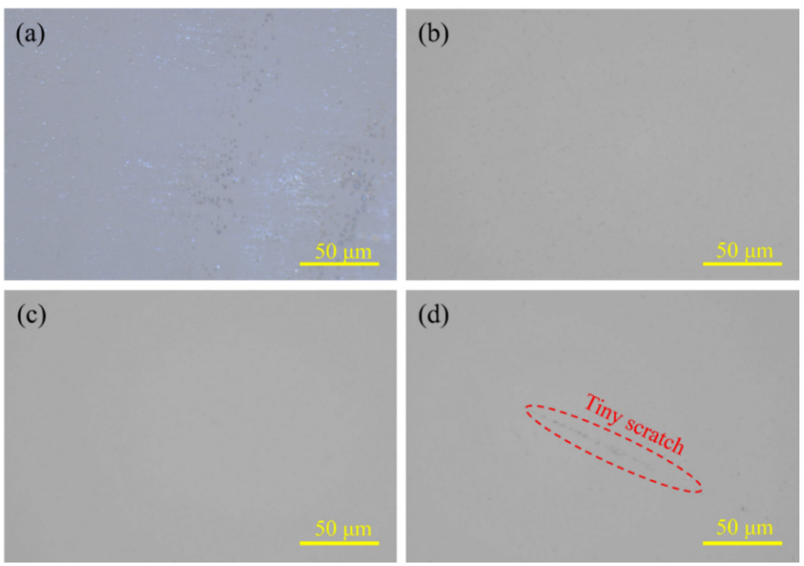

Fig. 6 Optical morphologies of different samples: (a) before polishing, (b) after S1 slurry-polishing, (c) after S2 slurry-polishing, (d) after S3 slurry-polishing.

Published on 04 January 2024. Downloaded by Yunnan University on 8/15/2025 7:01:03 AM.

constant force polishing procedure. (3) The rigid layer was precisely controlled to drive the abrasive in a negative direction along the X axis at a velocity of 40 m s^{-1} for a duration of 200 ps. (4) The rigid layer was controlled to drive the abrasive to move to the initial position along the positive direction of the Z axis.

3. Results and discussion

3.1. Experimental results

Fig. 5(a) presents the SEM image of the abrasives selected in this work, where it can be seen the abrasive size was relatively uniform, and its size distribution is displayed in Fig. 5(b). Most of the abrasive sizes ranged from 290–350 nm and their average size was 319.54 μm. The microstructure of the nonwoven polishing pad fiber applied in this work is displayed in Fig. 5(c). The polishing pad consisted of bent fibers in different directions and a relatively large porosity existed between the fibers. Most of the pad fiber diameters ranged from 13–22 μm and their mean diameter was 17.64 μm, as presented in Fig. 5(d). In the entire polishing progress, the abrasives were adsorbed on the pad fibers (Fig. 5(e) and (f)) and thus came into contact with the workpiece, which led to material removal.

Fig. 5(g) exhibits the rheology properties of the three developed slurries, and all the slurry samples exhibited a nonlinear rheology. The S1 slurry showed an obvious shear thickening property and its viscosity changed from 0.025 to 19.75 Pa s in a wide range of shear rates. When CMC-Na was introduced to the slurry, the S2 and S3 slurries displayed higher initial viscosities. At a relatively lower strain rate, the S2 and S3 samples showed an obvious shear thinning property and their viscosities dropped exponentially. When the lowest value was reached, their viscosities gradually increased and thus they

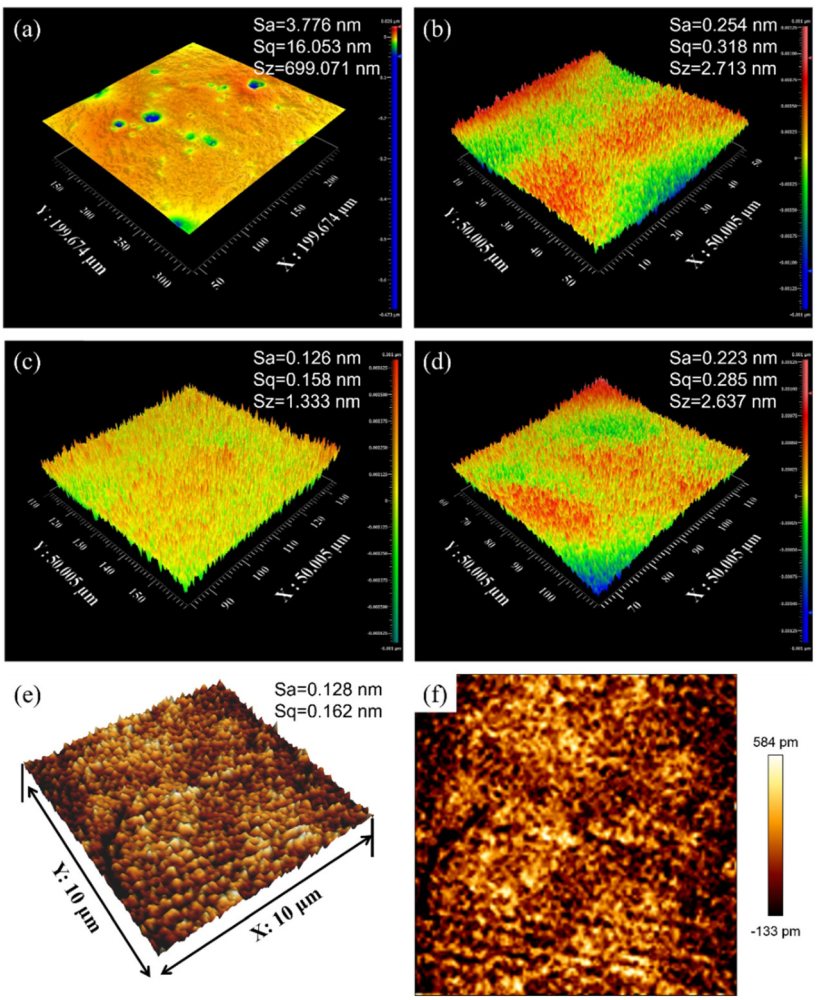

Fig. 7 Surface roughnesses of different samples measured by Zygo profilometry and AFM: (a) Before polishing, (b) after S1 slurry-polishing, (c) after S2 slurry-polishing, (d) after S3 slurry-polishing. (e) 3D AFM surface roughness after S2 slurry-polishing, (f) 2D AFM surface roughness after S2 slurry-polishing.

 This journal is © The Royal Society of Chemistry 2024

Published on 04 January 2024. Downloaded by Yunnan University on 8/15/2025 7:01:03 AM.

exhibited a shear thickening phenomenon. In general, the introduction of CMC-Na was conducive to improving the overall dynamic viscosity of the slurry.

The optical morphology of the rough- and fine-polished samples polished by different slurries are shown in Fig. 6 and their corresponding surface roughnesses are presented in

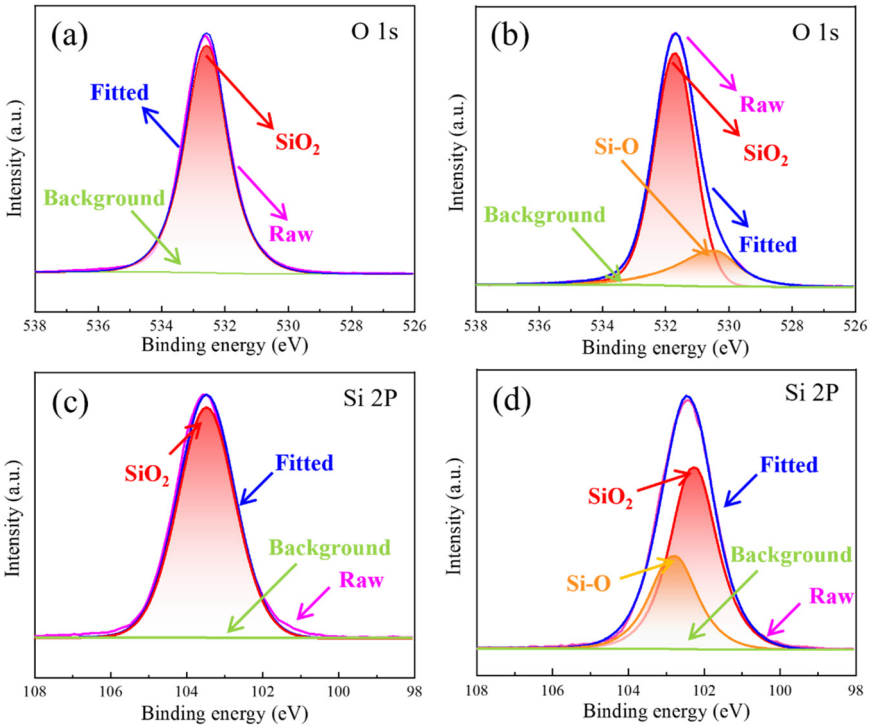

Fig. 8 XPS spectra of the samples: (a) O 1s XPS spectra of the rough-polished samples, (b) O 1s XPS spectra of the S2 slurry-polished samples, (c) Si 2P XPS spectra of the unpolished samples, (d) Si 2p XPS spectra of the S2 slurry-polished samples.

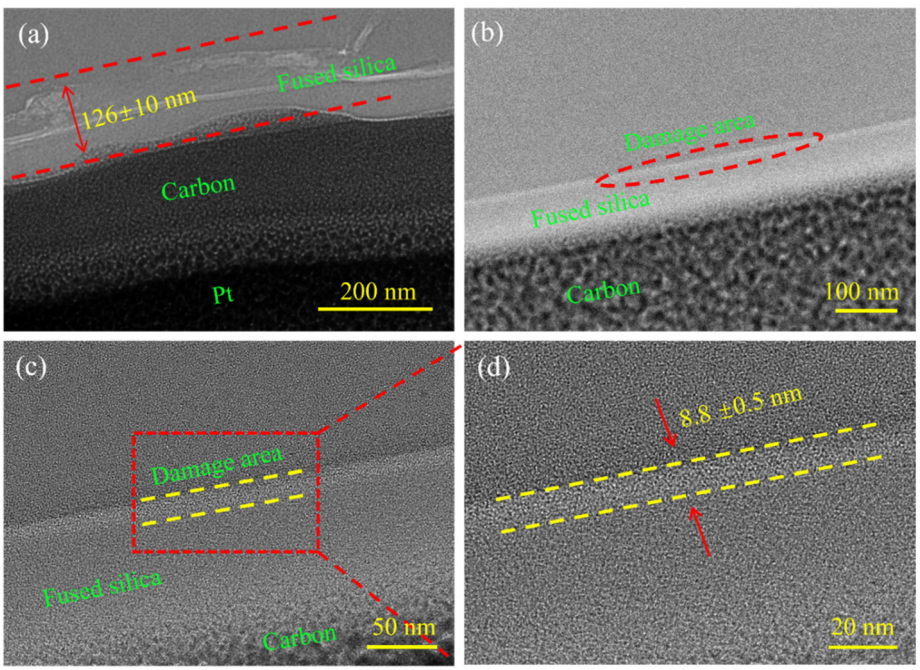

Fig. 9 Cross-sectional TEM images of the samples: (a) before fine polishing the samples, (b)–(d) after S2 slurry polishing the samples in different magnifications.

Published on 04 January 2024. Downloaded by Yunnan University on 8/15/2025 7:01:03 AM.

Fig. 7. The unpolished sample was terribly scratched and S_a value was 3.776 ± 0.92 nm, as shown in Fig. 7(a). After the CMP experiment, the fused silica surface roughness was significantly improved, and S_a values of 0.254 ± 0.42 nm, 0.126 ± 0.29 nm, and 0.223 ± 0.38 nm were obtained by the S1, S2, and S3 slurries as presented in Fig. 7(b)–(d), respectively. However, even though the surface had reached atomic-level roughness, a few tiny scratches were observed on the S3 sample surface, which resulted from the increase in dynamic viscosity of the slurry. To further verify the results, the 2D and 3D AFM surface roughnesses of the S2 slurry sample are shown in Fig. 7(e) and (f). The AFM results were consistent with the Zygo results, whereby S_a and S_q were 0.128 nm and 0.162 nm with a scanning range of 10 × 10 μm^2. From the perspective of the material-removal rate (MRR) shown in Fig. 5(h), with the increase in viscosity, the MRR was improved synchronously, and the S3 sample (123.8 ± 20.6 nm min^{-1}) demonstrated a 36.27% and 91.05% higher MRR than the S2 and S1 samples, respectively, at 88.3 ± 19.8 and 64.8 ± 15.6 nm min^{-1}.

Fig. 5(i) presents the infrared spectra of the rough-polished and fine-polished samples for the different slurries. It can be seen that similar trends occurred for the three fine-polished S1–S3 samples. The symmetrical tensile peaks at 780 and 1122 cm^{-1} belonged to the signal of Si–O–Si. The tensile vibration at 958 cm^{-1} resulted from Si–O. According to previous work, two essential stages for removing atoms from fused silica are experienced, namely the Si(substrate)–O–Si (abrasive) bridge bonds, and the breaking of the surrounding chemical bonds under bridge bond pulling. The reaction equations can be expressed by:[56,57]

$$H_2O \rightleftharpoons H^+ + OH^- \quad (16)$$

$$(\equiv Si)^+ + OH^- \rightleftharpoons (\equiv Si - OH) \quad (17)$$

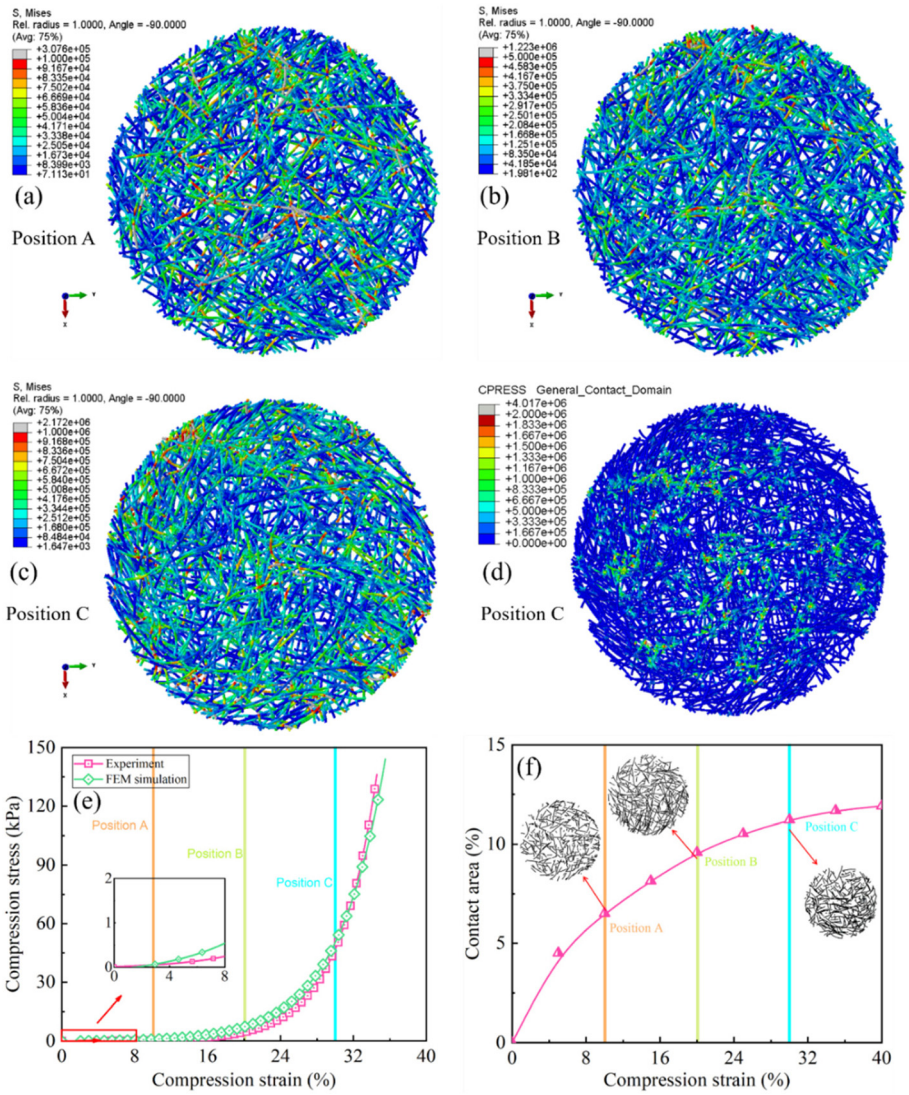

Fig. 10 (a)–(c) Stress distribution of the neat polishing pad under different compression strains; (d) contact pressure distribution between the pad fibers at position C; (e) compression stress–strain curve of the polishing pad; (f) direct contact area–compression strain curve of the fiber model.

This journal is © The Royal Society of Chemistry 2024

Published on 04 January 2024. Downloaded by Yunnan University on 8/15/2025 7:01:03 AM.

$$(\equiv Si-O)^- + H^+ \rightleftharpoons (\equiv Si-OH) \quad (18)$$

$$(\equiv Si)^+ + (\equiv Si-OH) \rightleftharpoons (\equiv Si-O-Si\equiv) + H^+ \quad (19)$$

$$H_3O^+ \rightleftharpoons H^+ + H_2O \quad (20)$$

From the perspective of the infrared peaks, with the increase in the slurry dynamic viscosity, the peaks of Si–O–Si and Si–O were more intense, which demonstrated that a higher viscosity will accelerate the formation of Si(substrate)–O–Si(abrasive) bridge bonds, thus further contributing to a higher MRR.

To further investigate and validate the material-removal mechanism in the CMP, XPS and cross-sectional TEM tests were conducted for the unpolished and S2 samples. The fine spectra of O 1s and Si 2p of the samples are shown in Fig. 8. As presented in Fig. 8(a) and (c), the fine spectra of O 1s and Si 2p of the unpolished fused silica showed a neat peak belonging to SiO_2. Fig. 8(b) is the fine O 1s spectrum of the S2-polished sample. In addition to the peak of SiO_2 at 531.84 eV, an extra peak of Si–O appeared at the binding energy of 530.62 eV. Similarly, the signal peak of Si–O was also observed at 102.7 eV in the Si 2p spectrum of the S2-polished sample, as shown in Fig. 8(d), which probably resulted from the generation of Si(substrate)–O–Si(abrasive) bridge bonds and also proved that the chemical reaction occurred on the surface of fused silica when contacted with the slurry.

Fig. 9 shows the fused silica cross-sectional TEM images before and after S2 slurry polishing. As can be seen from Fig. 9(a), the unpolished fused silica surface exhibited an approximately 126 ± 10 nm damage layer. After S2 fine CMP, the microcracks on the sub-surface were eliminated, and the damage layer thickness was reduced by 8.8 ± 0.5 nm, which was different from the nanostructure of the base fused silica. Therefore, the developed slurry in this work was highly efficient with ultralow damage.

3.2. Numerical results

3.2.1. Large-sized polishing pad fiber model. The microscopic contact state between the polishing pad and the workpiece has a great influence on the CMP performance. To the best of our knowledge, there is no numerical model yet that can fully predict and investigate the local and global complex nonlinear behaviors of complex working conditions. In this section, the fiber model was first applied for establishing the polishing model shown in Fig. 10. Fig. 10(a)–(c) display the neat pad stress distributions under 10%, 20%, and 30% compression strain marked as positions A, B, and C, respectively. It can be seen from Fig. 10(a)–(c) that as compression was conducted, the maximum and average stresses of the pad were significantly increased. When the pad was at position A, the maximum stress between the fibers was just 3.076×10^5 Pa and occurred at the intersection of the fibers. With the interaction between the fibers, the pressure at most of the load-

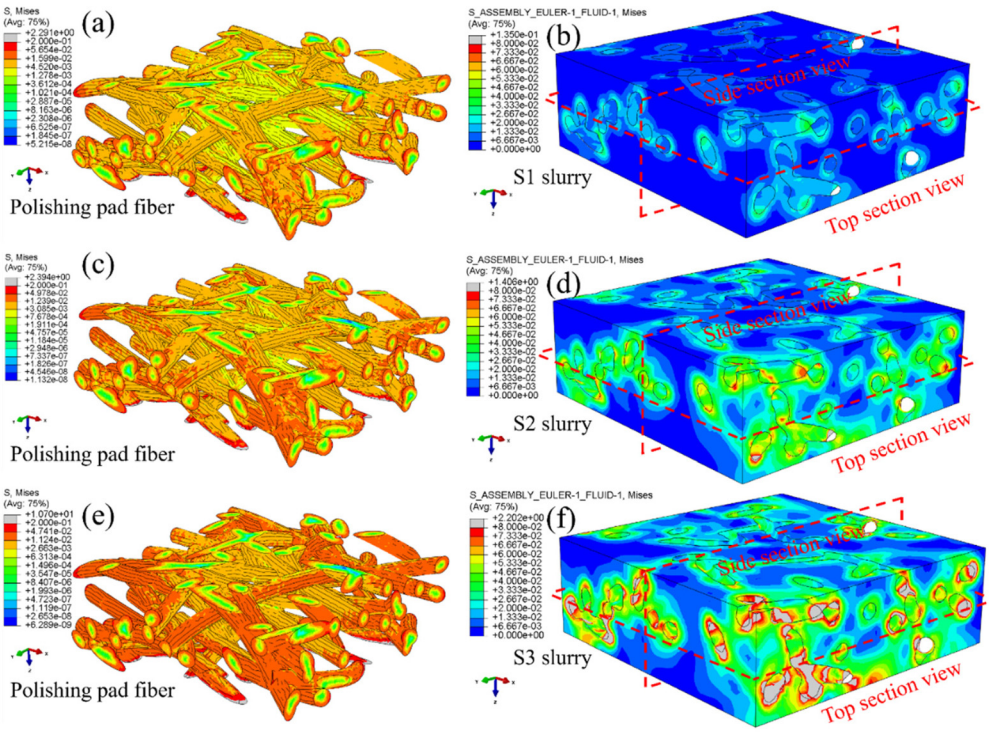

Fig. 11 CEL stress distribution of polishing pad fibers and different slurries under actual polishing conditions: (a) S1 sample pad stress distribution, (b) S1 sample slurry stress distribution, (c) S2 sample pad stress distribution, (d) S2 sample slurry stress distribution, (e) S3 sample pad stress distribution, (f) S3 sample slurry stress distribution.

Published on 04 January 2024. Downloaded by Yunnan University on 8/15/2025 7:01:03 AM.

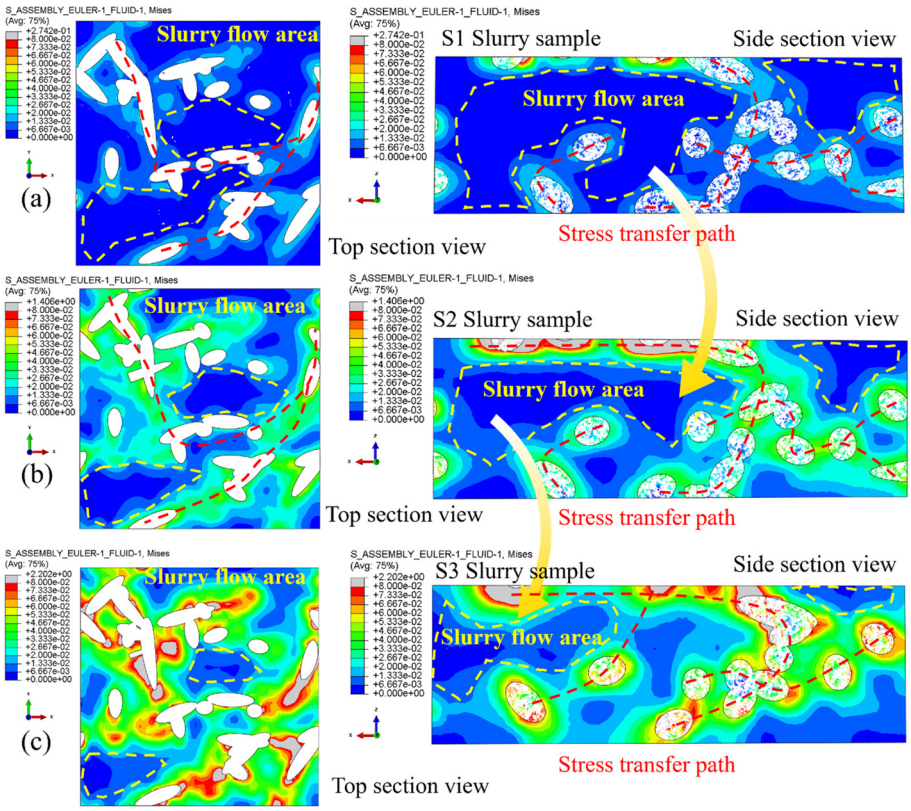

Fig. 12 Stress distribution of different slurries in different section views: (a) stress distribution of the S1 slurry in top and side section views, (b) stress distribution of the S2 slurry in top and side section views, (c) stress distribution of the S3 slurry in top and side section views.

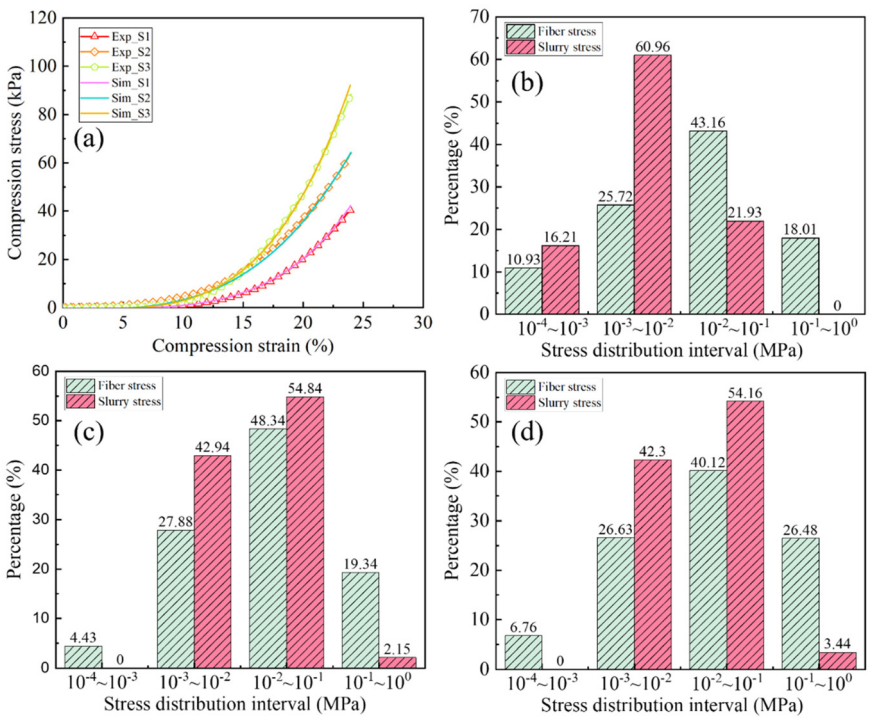

Fig. 13 (a) Experimental and numerical compression stress–strain curves of different slurry samples. (b) Stress distribution intervals of the fiber and slurry for the S1 sample, (b) stress distribution intervals of the fiber and slurry for the S2 sample, (c) stress distribution intervals of the fiber and slurry for the S3 sample.

This journal is © The Royal Society of Chemistry 2024

Published on 04 January 2024. Downloaded by Yunnan University on 8/15/2025 7:01:03 AM.

bearing fibers ranged from 10^4 to 10^5 Pa. When the compression strain was increased to 20% (Position B), the stress level between the fibers increased by orders of magnitude and the maximum stress reached 1.223×10^6 Pa. When the strain reached 30%, the stress between the fibers did not change by an order of magnitude as before and most fibers were still at the 10^5 Pa level. However, the fibers gradually became curly and deformed, thus leading to the subsequent loading of more fibers.

Fig. 10(d) displays the internal contact pressure between the pad fibers. In general, the contacts between the non-woven pad fibers were highly nonlinear and the large pressure area was concentrated in the direct contact area between the fibers. Fig. 10(e) shows the compression stress–strain curve of the polishing pad, where the curve also exhibited an obvious nonlinear characteristic, showing the experiment and fiber model results were in good agreement. When the compression strain was lower than 20%, the pad displayed a lower elastic modulus. However, greater than 30% strain, the compacted state was reached and the curve showed a sharp increase in stiffness. The real contact area of the polishing pad is an important bacteriostatic for CMP quantitative analysis, which is influenced by the pad microstructure and fiber properties. When the contact area is higher, the point stress of the workpiece is lower, and surface scratches can be effectively avoided. Fig. 10(f) shows the real contact area between the pad and workpiece under different compression strains (the part with less than 1 μm from the workpiece is considered the real contact). The contact curve showed a rapid increase in contact area under low compression strain. When the polishing pad was compacted, the curve slope of the curve decreased, and the increment of the contact area tended to be flat, which significantly deviated from the previously proposed linear computational model. Under actual polishing conditions (37.5 kPa), the direct contact area was 11.12%. Through the fiber model, the microscopic contact state of the polishing pads could be more fully characterized.

3.2.2. Mesoscale numerical analysis. Limited by the complexity and difficulty of the nonlinear computation, few works have been devoted to investigating the coupling effect of polishing pad fibers and slurries. In this section, the CEL approach was first applied to further explore their interaction under actual polishing conditions for different developed slurries. Fig. 11 shows the CEL numerical stress distribution of the polishing pad fibers and different slurries under experimental polishing conditions. In general, it could be concluded that

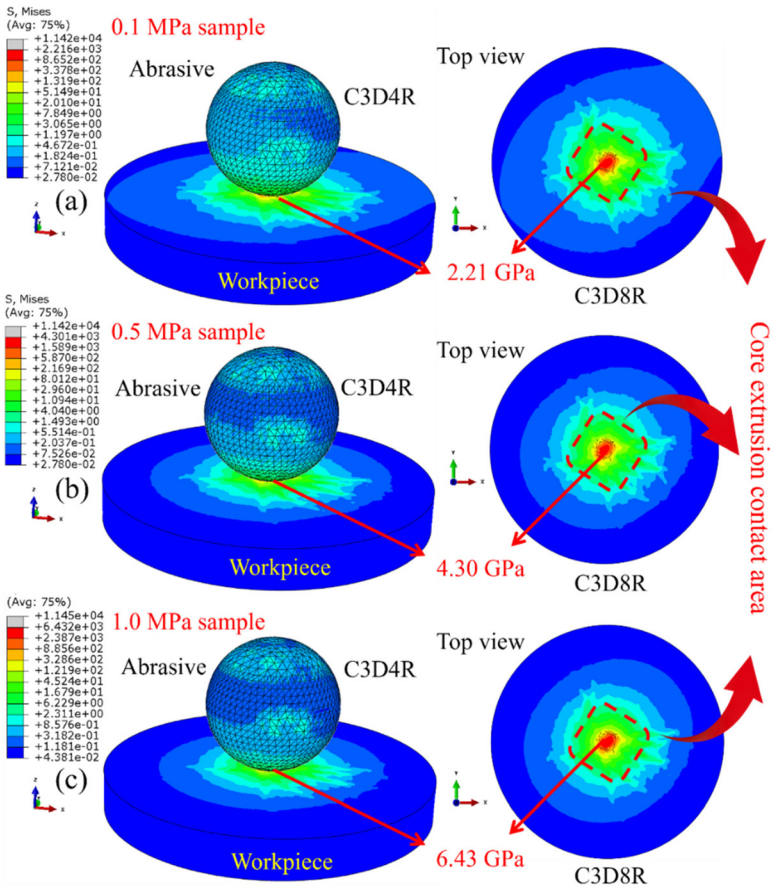

Fig. 14 Stress distributions of the abrasives and workpiece for different loading boundary conditions: (a) 0.1 MPa sample, (b) 0.5 MPa sample, (c) 1.0 MPa sample.

Published on 04 January 2024. Downloaded by Yunnan University on 8/15/2025 7:01:03 AM.

the pad fiber stress was an order of magnitude greater than the slurry. With the increase in the polishing slurry viscosity, the stress level of the fiber gradually increased (Fig. 11(a), (c), and (e)). The stress level of the fiber shell layer was significantly higher than the core layer, indicating the strong FSI coupling effect. For the polishing pad fiber, the stress level around the fiber was significantly higher than that far beyond the fiber, which proved the existence of the fiber was conducive to stress transfer and diffusion. Similarly, the slurry viscosity increase exhibited a great effect on the macroscopic stress, whereby the highest stress was concentrated at the junctions between fibers.

Fig. 12 presents the stress distribution of slurries in different section views for the different samples. From the section views, the presence of fibers was crucial for the effective distribution and transmission of both longitudinal and transverse stresses (Fig. 12(a)–(c)). The overall stress at the intersections of multiple fibers was significantly higher than at the other parts, which demonstrated that in addition to the fibers, the fluid loading induced by the fiber connections also conferred advantages for material removal, which was consistent with the MRR in Fig. 5(h). However, the increase in viscosity led to a drop in low stress areas, which demonstrated that while higher viscosity enhances the stress level and facilitates the material removal, excessive viscosity can impair low stress regions and compromise the slurry fluidity, leading to the accumulation of abrasives and the generation of large scratches, as shown in Fig. 6(d).

Fig. 13(a) displays the experimental and numerical compression stress–strain curves of the different slurry samples. It can be seen that the simulated data were in good agreement with the experimental curve, which further substantiated the accuracy of the model on the basis of the large-sized polishing pad model. The increase in slurry viscosity led to a significant enhancement in the stiffness of the polishing pad after infiltration. To further investigate the fluid loading mechanism, the percentages of elements in different stress distribution intervals for the fibers and slurry in the mesoscale model were collected and are shown in Fig. 13(b)–(d). For the S1 slurry sample, 43.16% of the fiber element stress was in the 10^{-2}–10^{-1} MPa interval, while 60.96% of the slurry element was concentrated in the 10^{-3}–10^{-2} interval MPa. For a greater stress interval of 10^{-1}–10^{0} MPa interval, 18.01% of the fiber elements accounted for the whole, while the slurry elements reached this interval, which proved that the loading and material-removal mechanism of the S1 sample were mainly provided by the fibers. When the slurry viscosity further increased, the overall element stress was obviously improved and 19.34% of fiber elements were in the 10^{-1}–10^{0} MPa interval. Most of the slurry elements' (54.84%) stress levels changed from 10^{-3}–10^{-2}

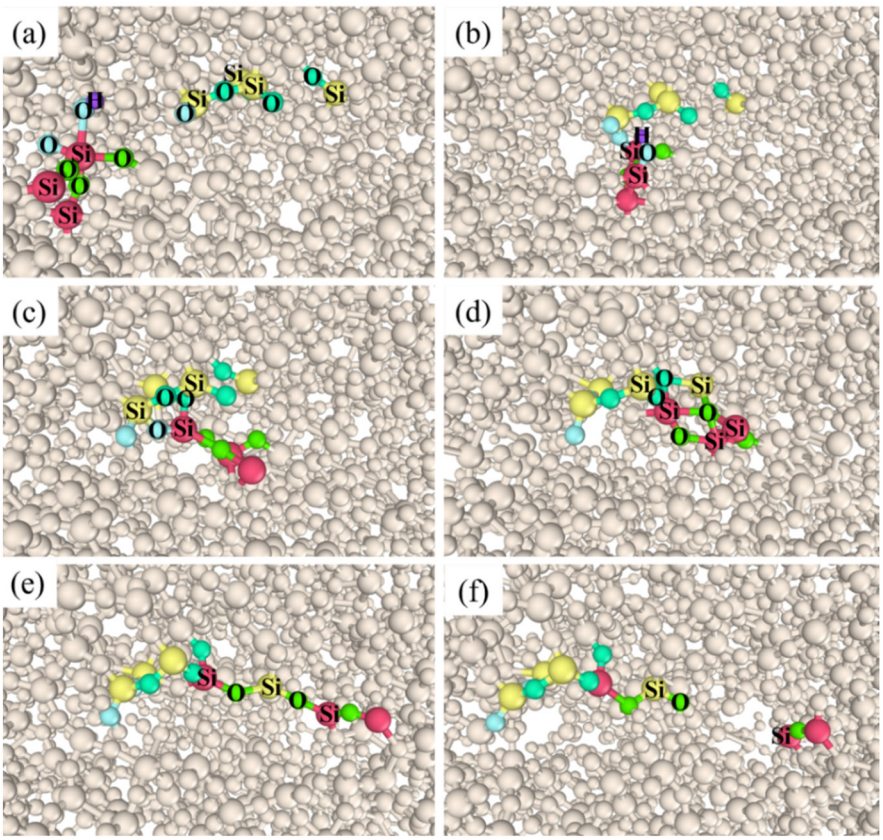

Fig. 15 Dynamic removal of atoms from the workpiece: (a)–(d) Formation of Si–O–Si bridge bonds, (e) and (f) dynamic breaking of the chemical bonds under the pulling of the bridge bonds.

 This journal is © The Royal Society of Chemistry 2024

Published on 04 January 2024. Downloaded by Yunnan University on 8/15/2025 7:01:03 AM.

to 10^{-2}–10^{-1} MPa intervals, which proved that the increase in viscosity contributed to the enhancement of the slurry overall stress interval and thus could reduce the point contact between the fiber and workpiece, thereby facilitating a uniform load bearing between the polishing pad fiber and workpiece. For the highest viscosity S3 sample, 26.48% of the fiber elements and 3.44% of the slurry elements achieved the maximum 10^{-1}–10^{0} MPa interval. The significant increase in stress levels of the above elements resulted in the further increase in the overall MRR, as presented in Fig. 5(h). Therefore, in the next section, the three typical stresses (10^{-1}, 5 × 10^{-1}, 10^{0}) of the maximum stress interval were selected as abrasive boundary conditions to explore the abrasive–workpiece interaction.

3.2.3. Microscale and nanoscale numerical results. In this section, the typical stress was applied to explore the interaction between the abrasive and workpiece. Fig. 14 reveals the stress distributions in different views. It can be seen that the maximum stress was produced by the direct contact area and then the stress radially diverged. After removing the stress singular value, the maximum stress values generated by the workpiece surface were 2.21, 4.30, and 6.43 Gpa. Through calculation of the abrasive and workpiece in this step, the stress on the workpiece was precisely obtained. Then, the stress on the workpiece was extracted as an input boundary condition for ReaxFF-MD to further investigate the atomic-level material-removal mechanism. The above analysis at different scales mainly focused on the mechanical mechanism between the different parts. However, the chemical reactions between the abrasive–slurry–workpiece interface are still unclear.

Fig. 15 reveals the group of typical dynamic atom removal progress steps based on ReaxFF-MD. Previous research has demonstrated that there are two fundamental stages of removing atoms from fused silica; namely, the formation of Si(substrate)–O–Si(abrasive) and the breaking of chemical bonds under the pulling of bridge bonds A, as described in eqn (16)–(20). Fig. 10(a)–(d) illustrate the formation of Si(substrate)–O–Si(abrasive). Under the coupling effect of the sliding action

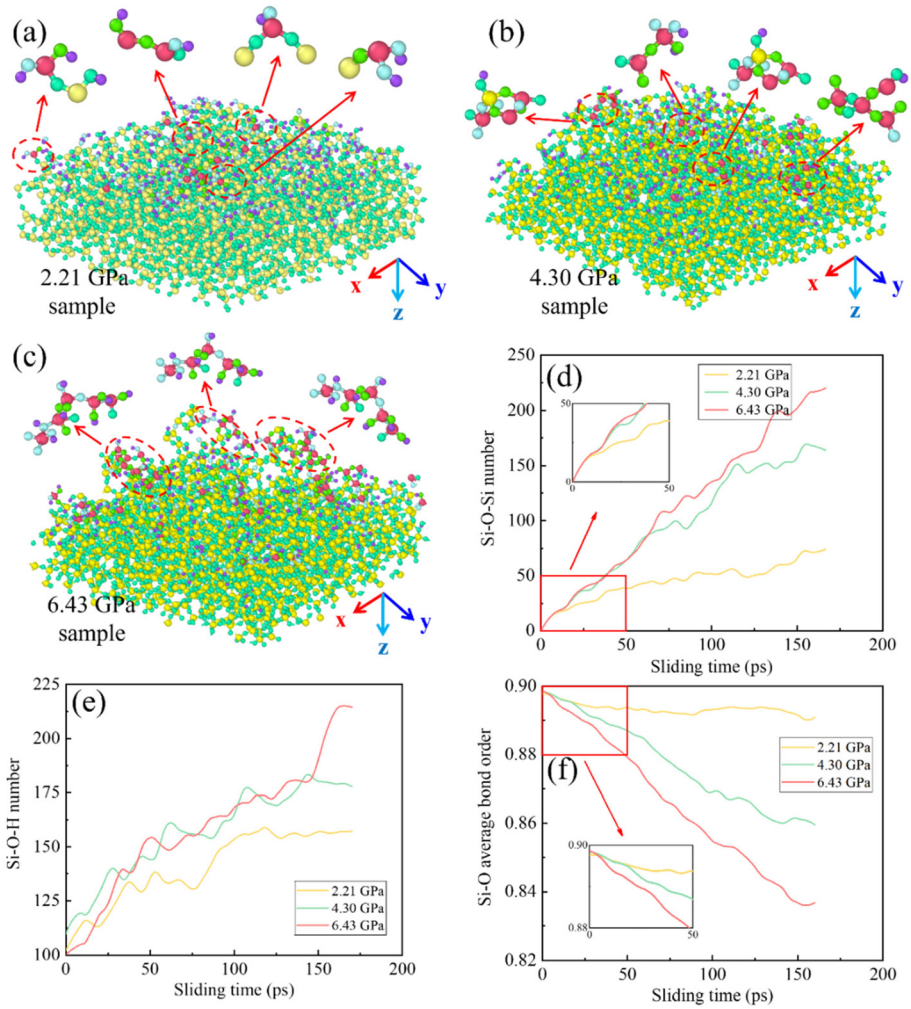

Fig. 16 Surface atomic chemical states of the abrasive after sliding for different samples: (a) 2.21 GPa sample, (b) 4.30 GPa sample, (c) 6.43 GPa sample, (d) Si–O–Si number–sliding time curves, (b) Si–O–H number–sliding time curves, (f) Si–O average bond order.

Published on 04 January 2024. Downloaded by Yunnan University on 8/15/2025 7:01:03 AM.

and surrounding atoms, the Si(abrasive) and Si(substrate) experience dehydroxylation and dehydrogenation reactions and thus the Si(abrasive)–O–Si(substrate) bonds were formed, as shown in Fig. 15(e) and (f), which display the pulling breaking bonds of Si(substrate)–O–Si(abrasive). Therefore, the bridge bond number and chemical bond stability were the most significant factors affecting the material removal.

To further investigate the atomic chemical state in the CMP, the atomic distributions after sliding under different pressures were obtained as presented in Fig. 16(a)–(c). The interface stress had a great significance on bridge bond formation, thus further affecting the removal mechanism. Under the lower 2.21 GPa pressure, only a few bridge bonds between the abrasive, slurry, and workpiece were generated, resulting in only 1–2 Si atoms being removed, which was considered as single-atom removal. For the 4.30 GPa pressure sample (Fig. 16(b)), 2–4 adjacent Si atoms were removed in the molecular chain by the generation of more bridges bonds between the workpiece and slurry. When the pressure was increased to 6.43 GPa, the removed number of atoms improved sharply, as presented in Fig. 16(c), whereby the removal form was transformed into molecular chain removal, which confirmed the importance of bridge bond formation for material removal.

Fig. 16(d) shows the statistical Si–O–Si bridge bonds number–sliding time curve in the CMP process. Under 2.21 GPa pressure, only a small number of bridge bonds were generated during sliding. With the enhancement of the pressure, the number of bridge bonds increased sharply, which properly resulted from the interface response under different loadings. Under relatively lower pressure, the slurry layer at the interface blocked direct contact between the abrasive and fused silica. However, with the improvement of pressure, the blocking effect of water was significantly weakened. In the entire sliding process, the bridge bonds continued to form and break. In the CMP process, a large amount of free H^+ existed in aqueous H_2O_2, which affected the surface hydroxyl ratio. The O atoms of fused silica rapidly combined with free H^+ to form Si–OH bonds. Fig. 16(e) shows that as the pressure increased, the number of surface hydroxylation bonds also increased. The bond order indicated the strength of the chemical bonds between atoms. When the bond order value is larger, the bond between atoms is more stable and the possibility of bond breaking is less. Fig. 16(d) displays the average bond order–sliding time curves for different samples, while the 6.43 GPa sample average bond order was generally lower than the 4.30 GPa and 2.21 GPa samples, and the lowest value of 0.835 was reached at the end of the sliding.

4. Conclusion

CMP is considered as the foremost way to obtain global nanoscale flattening, and has been widely applied in optical fields and semiconductor manufacturing. In this work, an approach involving a full-scale mapping analysis strategy (from mm–nm) was first proposed to instigate the influence of nonlinear viscosity on the polishing performance in different scales combined with a designed environmentally friendly slurry containing H_2O_2, Na_2CO_3, CMC-Na, and spherical SiO_2 abrasive. An ultrasmooth and high-quality surface was obtained with 0.126 nm surface roughness, 8.8 nm damage layer thickness, and an 88.3 nm min^{-1} material-removal rate. In the full-scale analysis, the large-sized fiber model showed the nonlinear compression property of the neat non-woven polishing pad, while a 11.12% direct contact area was obtained under actual polishing condition in the macroscale. When the strain reached 30%, most fibers were at a 10^5 Pa level, and then the fibers gradually became curly and deformed, leading to the subsequent loading of more fibers. In the mesoscale, the CEL model revealed the overall stress at the intersection of multiple fibers was significantly higher than the slurry and most of the fiber elements were in the 10^{-2}–10^{-1} MPa interval. The increase in viscosity led to a drop in the low stress areas and demonstrated that a higher viscosity could enhance the stress level and facilitate material removal. For the microscale and nanoscale, the surface stresses of the abrasive on the workpiece were in the 2.21–6.43 GPa interval. The ReaxFF-MD model demonstrated that the interface stress has a great significance on bridge bond formation, thus further contributing to the removal mechanism. With the elevated compressive stress of the abrasive on the workpiece, the removal form changes from single atom to molecular chain removal. The full-scale analysis strategy proposed in this study can achieve a systematic logical mapping analysis across the macro, meso, micro, and nano scales, offering valuable guidance for future advancements in the design and development of CMP processes.

Author contributions

Z. Y. Z. conceived the projects. F. Z. performed the experiments and simulation. X. Q. D. and J. Y. F. analyzed the mechanism and completed the manuscript. H. X. Z., F. N. M. and C. J. S. revised the manuscript. F. N. M. and C. J. S. characterized the samples. All authors discussed the results.

Conflicts of interest

The authors declare no competing interests.

Acknowledgements

The authors acknowledge the financial supports from the National Key Research and Development Program of China (2018YFA0703400), the Basic Research Expenses for Provincial Colleges and Universities – Research and Innovation Project for Young Teachers (GK239909299001-021), the Young Scientists Fund of the National Natural Science Foundation of China (52205447), and the Changjiang Scholars Program of Chinese Ministry of Education.

 This journal is © The Royal Society of Chemistry 2024

Published on 04 January 2024. Downloaded by Yunnan University on 8/15/2025 7:01:03 AM.

References

1 Y. Liu, X. Duan, H.-J. Shin, S. Park, Y. Huang and X. Duan, *Nature*, 2021, **591**, 43–53.
2 F. P. García de Arquer, D. V. Talapin, V. I. Klimov, Y. Arakawa, M. Bayer and E. H. Sargent, *Science*, 2021, **373**, eaaz8541.
3 Z. Zhang, J. Yan and T. Kuriyagawa, *Int. J. Extreme Manuf.*, 2019, **1**, 022001.
4 Q. Sun, D. Yang, T. Liu, J. Liu, S. Wang, S. Hu, S. Liu and Y. Song, *Microsyst. Nanoeng.*, 2023, **9**, 50.
5 X. Wang, H. Zhang, T. Baba, H. Jiang, C. Liu, Y. Guan, O. Elleuch, T. Kuech, D. Morgan, J.-C. Idrobo, P. M. Voyles and I. Szlufarska, *Nat. Mater.*, 2020, **19**, 992–998.
6 W.-L. Zhu and A. Beaucamp, *Int. J. Mach. Tools Manuf.*, 2020, **158**, 103634.
7 Y. Xu, J. Lu, X. Xu, C.-C. A. Chen and Y. Lin, *Int. J. Mach. Tools Manuf.*, 2018, **130–131**, 12–19.
8 H. Luo, K. M. Ajmal, W. Liu, K. Yamamura and H. Deng, *Int. J. Extreme Manuf.*, 2021, **3**, 022003.
9 H. Ohmori, S. Umezu, Y. Kim, Y. Uehara, H. Kasuga, T. Kato, N. Itoh, S. Kurokawa, T. Kusumi, Y. Sugawara and S. Kunimura, *Int. J. Extreme Manuf.*, 2020, **2**, 015101.
10 Y. Wu, D. Mu and H. Huang, *Int. J. Extreme Manuf.*, 2020, **2**, 012006.
11 L. Wang, P. Zhou, Y. Yan and D. Guo, *Int. J. Mech. Sci.*, 2022, **230**, 107559.
12 P. Zhou, H. Shi, L. Wang, C. Hou, L. Meng, H. Di and D. Guo, *Int. J. Mech. Sci.*, 2023, **239**, 107878.
13 V. Valmacco, M. Elzbieciak-Wodka, C. Besnard, P. Maroni, G. Trefalt and M. Borkovec, *Int. J. Mech. Sci.*, 2016, **1**, 325–330.
14 W. Xie, Z. Zhang, L. Liao, J. Liu, H. Su, S. Wang and D. Guo, *Nanoscale*, 2020, **12**, 22518–22526.
15 X. Cui, Z. Zhang, S. Yu, X. Chen, C. Shi, H. Zhou, F. Meng, J. Yu and W. Wen, *Nanoscale*, 2023, **15**, 9304–9314.
16 J. Chen, Z. Lin, T. Jin, B. Liu and A. Nie, *Appl. Surf. Sci.*, 2023, **641**, 158500.
17 D. Liu, Z. Zhang, H. Zhou, X. Deng, C. Shi, F. Meng, Z. Yu and J. Feng, *Appl. Surf. Sci.*, 2023, **640**, 158382.
18 X. Shi, L. Xu, Y. Zhou, C. Zou, R. Wang and G. Pan, *Nanoscale*, 2018, **10**, 19692–19700.
19 M.-S. Pham, B. Dovgyy, P. A. Hooper, C. M. Gourlay and A. Piglione, *Nat. Commun.*, 2020, **11**, 749.
20 Q. Zhai, W. Zhai and T. Deng, *Appl. Surf. Sci.*, 2023, **619**, 156778.
21 K. C. Lin and C.-C. Liao, *Chem. Eng. Res. Des.*, 2023, **191**, 375–386.
22 J. Feng, Z. Zhang, S. Yu, X. Chen, D. Wang, Q. Gu, C. Zhou, T. Zhang and B. Liu, *Addit. Manuf.*, 2023, **72**, 103634.
23 C. J. Wang, C. F. Cheung, L. T. Ho, M. Y. Liu and W. B. Lee, *Int. J. Mach. Tools Manuf.*, 2017, **115**, 60–73.
24 H.-M. Ding and Y.-Q. Ma, *Nanoscale Horiz.*, 2018, **3**, 6–27.
25 N. Duan, Y. Yu, W. Wang and X. Xu, *Int. J. Mach. Tools Manuf.*, 2017, **120**, 49–60.
26 S. Zhang and W. Zong, *Int. J. Mech. Sci.*, 2021, **196**, 106271.
27 J. Zhao, S. Zhao and S. Luding, *Nat. Rev. Phys.*, 2023, **5**, 505–525.
28 Y. Pan, Y. Zhang, P. Gongpan, Q. Zhang, S. Huang, B. Wang, B. Xu, Y. Shan, W. Xiong, G. Li and H. Wang, *Nanoscale Horiz.*, 2018, **3**, 517–524.
29 G. Wang, Z. Feng, Q. Zheng, B. Li and H. Zhou, *Mater. Sci. Semicond. Process.*, 2020, **118**, 105168.
30 Q. Liang, M. Bartnof, Y.-L. He, J. A. Malen and A. J. H. McGaughey, *Nanoscale Horiz.*, 2020, **5**, 1524–1529.
31 J. Feng and Z. Guo, *Nanoscale Horiz.*, 2019, **4**, 339–364.
32 J. Zhang, R. Hong and H. Wang, *Addit. Manuf.*, 2022, **59**, 103152.
33 L. Wang, P. Zhou, Y. Yan, R. Kang and D. Guo, *Tribol. Int.*, 2019, **138**, 307–315.
34 V.-T. Nguyen and T.-H. Fang, *Thin Solid Films*, 2021, **731**, 138744.
35 J. Zhu, J. Wang, W. Han and D. Xu, *Nat. Commun.*, 2022, **13**, 1661.
36 H. Lu, Y. Liu, P. Ahlawat, A. Mishra, W. R. Tress, F. T. Eickemeyer, Y. Yang, F. Fu, Z. Wang, C. E. Avalos, B. I. Carlsen, A. Agarwalla, X. Zhang, X. Li, Y. Zhan, S. M. Zakeeruddin, L. Emsley, U. Rothlisberger, L. Zheng, A. Hagfeldt and M. Grätzel, *Science*, 2020, **370**, eabb8985.
37 S. Naserifar, Y. Chen, S. Kwon, H. Xiao and W. A. Goddard, *Matter*, 2021, **4**, 195–216.
38 A. Karuth, A. Alesadi, A. Vashisth, W. Xia and B. Rasulev, *ACS Appl. Polym. Mater.*, 2022, **4**, 4411–4423.
39 X. Guo, S. Yuan, Y. Gou, X. Wang, J. Guo, Z. Jin and R. Kang, *Appl. Surf. Sci.*, 2020, **508**, 145262.
40 X. Guo, S. Yuan, J. Huang, C.-F. Chen, R. Kang, Z. Jin and D. Guo, *Appl. Surf. Sci.*, 2020, **505**, 144610.
41 J. Wen, T. Ma, W. Zhang, A. C. T. van Duin, D. M. van Duin, Y.-Z. Hu and X. Lu, *J. Phys. Chem. C*, 2019, **126**, 26467–26474.
42 S. Yuan, X. Guo, S. Zhang, C. Zhang, P. Li, Z. Jin, R. Kang and D. Guo, *Appl. Surf. Sci.*, 2021, **566**, 150638.
43 J.-Z. Jiang, Y.-W. Zhao, Y.-G. Wang and J.-B. Luo, *Wear*, 2008, **265**, 992–998.
44 H. Lee and H. Jeong, *Int. J. Mach. Tools Manuf.*, 2011, **51**, 395–403.
45 M. Uneda, Y. Maeda, K.-I. Ishikawa, K. Ichikawa, T. Doi, T. Yamazaki and H. Aida, *J. Electrochem. Soc.*, 2011, **159**, H90.
46 F. Zhao, L. Wu, Z. Lu, J.-H. Lin and Q. Jiang, *Mater. Des.*, 2022, **213**, 110375.
47 S. Sen, M. N. B. Jamal, A. Shaw and A. Deb, *Int. J. Mech. Sci.*, 2019, **164**, 105174.
48 G. Eskandarnia and P. Soltani, *Geotext. Geomembr.*, 2023, **51**, 1–14.
49 T. G. Zieliński, *J. Sound Vib.*, 2017, **409**, 112–130.
50 Y. He, N. Deng, B. Xin and L. Liu, *Micron*, 2021, **144**, 103035.
51 P. Du, X. Ding, Q. Liang, X. Chen, Y. Zhang and L. Chen, *Text. Res. J.*, 2022, **92**, 2100–2111.
52 L. Wu, F. Zhao, J. Xie, X. Wu, Q. Jiang and J.-H. Lin, *Int. J. Mech. Sci.*, 2020, **187**, 105929.
53 Z. Lu, L. Wu, B. Gu and B. Sun, *Composites, Part B*, 2015, **69**, 191–200.

54 Y. Jin, Y. Wang, X. Zhang and B. Wang, *J. Mater. Process. Technol.*, 2020, **285**, 116786.
55 M. R. I. Islam, J. Q. Zheng and R. C. Batra, *Int. J. Impact Eng.*, 2020, **137**, 103469.
56 W. Ma, J. Li and X. Hou, *Int. J. Mech. Sci.*, 2023, **258**, 108572.
57 X. Wang, S. H. Kim, C. Chen, L. Chen, H. He and L. Qian, *ACS Appl. Mater. Interfaces*, 2015, **7**, 14785–14792.

Published on 04 January 2024. Downloaded by Yunnan University on 8/15/2025 7:01:03 AM.

This journal is © The Royal Society of Chemistry 2024